

EZH2 is a potential therapeutic target for H3K27M-mutant pediatric gliomas

Faizaan Mohammad^{1,2}, Simon Weissmann^{1,2,9}, Benjamin Leblanc^{1-3,9}, Deo P Pandey^{1,2,9}, Jonas W Højfeldt^{1,2}, Itys Comet^{1,2}, Chunqin Zheng^{1,2}, Jens Vilstrup Johansen¹, Nicolas Rapin^{1,3-5}, Bo T Porse^{1,3,4}, Andrey Tvardovskiy^{2,6}, Ole N Jensen^{2,6}, Nagore G Olaciregui⁷, Cinzia Lavarino⁷, Mariona Suñol⁸, Carmen de Torres⁷, Jaume Mora⁷, Angel M Carcaboso⁷ & Kristian Helin¹⁻³

Diffuse intrinsic pontine glioma (DIPG) is an aggressive brain tumor that is located in the pons and primarily affects children. Nearly 80% of DIPGs harbor mutations in histone H3 genes, wherein lysine 27 is substituted with methionine (H3K27M). H3K27M has been shown to inhibit polycomb repressive complex 2 (PRC2), a multiprotein complex responsible for the methylation of H3 at lysine 27 (H3K27me), by binding to its catalytic subunit EZH2. Although DIPGs with the H3K27M mutation show global loss of H3K27me3, several genes retain H3K27me3. Here we describe a mouse model of DIPG in which H3K27M potentiates tumorigenesis. Using this model and primary patient-derived DIPG cell lines, we show that H3K27M-expressing tumors require PRC2 for proliferation. Furthermore, we demonstrate that small-molecule EZH2 inhibitors abolish tumor cell growth through a mechanism that is dependent on the induction of the tumor-suppressor protein p16^{INK4A}. Genome-wide enrichment analyses show that the genes that retain H3K27me3 in H3K27M cells are strong polycomb targets. Furthermore, we find a highly significant overlap between genes that retain H3K27me3 in the DIPG mouse model and in human primary DIPGs expressing H3K27M. Taken together, these results show that residual PRC2 activity is required for the proliferation of H3K27M-expressing DIPGs, and that inhibition of EZH2 is a potential therapeutic strategy for the treatment of these tumors.

EZH2 is amplified and/or overexpressed in a variety of solid tumors, including prostate, kidney, breast and colorectal cancer, and elevated *EZH2* activity in tumors is associated with poor prognosis^{1,2}. In addition, somatic activating point mutations of *EZH2* have been identified in non-Hodgkin's lymphoma, which suggests that increased PRC2 activity is a recurrent event in cancers¹⁻⁵. These observations have provided an impetus for the development of *EZH2* inhibitors as potential anti-cancer drugs, which are now in clinical trials⁶⁻⁹. However, inactivating mutations in *EZH2* have also been reported in myeloproliferative disorders and T cell acute lymphoblastic leukemia, demonstrating that *EZH2* also has tumor-suppressive functions^{10,11}.

Recently, an additional mechanism through which cancer cells can modulate PRC2 activity was found in DIPGs. Among primary brain tumors in children, DIPGs have the worst prognosis, and despite huge efforts to improve treatment, the outcome of current therapies remains dismal, with a median overall survival of only 8–11 months after diagnosis^{12,13}. Up to 80% of DIPGs harbor a mutation in canonical (*HIST1H3B* (H3.1)) or variant (*H3F3A* (H3.3)) histone H3, leading to the expression of H3K27M¹⁴⁻¹⁸. H3K27M has been shown to inhibit PRC2 activity, and DIPGs expressing H3K27M mutant show global reduction of H3K27me3 levels¹⁹. Considering that the

H3K27M mutation occurs in a single allele of a total of 30 copies of histone H3 genes, and that mutant H3K27M therefore constitutes a minor part (3.6% to 17.6%)¹⁹ of total H3 protein in DIPGs, this indicates that H3K27M inhibits PRC2 activity. However, the analyses of global distribution of H3K27me3 have shown that a substantial number of genes retain H3K27me3 in H3K27M-mutant DIPGs^{20,21}. How H3K27M affects global H3K27me3 levels and how it contributes to tumor development are not yet fully understood.

To understand the role of H3K27M in DIPGs, we developed a mouse model of DIPG in which H3K27M potentiates platelet-derived growth factor (PDGF) subunit B (PDGFB)-driven tumor development. By using this model, as well as patient-derived DIPG cell lines, we show here that the residual PRC2 activity in H3K27M-mutant DIPGs is required for tumor growth. Moreover, we provide a mechanism to explain why these tumors are dependent on PRC2 activity and why H3K27me3 is retained at several genes.

RESULTS

H3K27M potentiates tumor development in mice

Increased PDGF signaling or mutation in *TP53* (also known as *TRP53*) is frequently associated with H3K27M-mutant expression in

¹Biotech Research and Innovation Centre (BRIC), University of Copenhagen, Copenhagen, Denmark. ²Centre for Epigenetics, University of Copenhagen, Copenhagen, Denmark. ³The Danish Stem Cell Center (Danstem), University of Copenhagen, Faculty of Health and Medical Sciences, University of Copenhagen, Copenhagen, Denmark. ⁴The Finsen Laboratory, Rigshospitalet, Faculty of Health and Medical Sciences, University of Copenhagen, Copenhagen, Denmark. ⁵The Bioinformatics Centre, Department of Biology, University of Copenhagen, Copenhagen, Denmark. ⁶Department of Biochemistry and Molecular Biology, VILLUM Center for Bioanalytical Sciences, University of Southern Denmark, Odense M, Denmark. ⁷Department of Pediatric Hematology and Oncology, Hospital Sant Joan de Déu Barcelona, Barcelona, Spain. ⁸Pathology, Hospital Sant Joan de Déu Barcelona, Barcelona, Spain. ⁹These authors contributed equally to this work. Correspondence should be addressed to K.H. (kristian.helin@bric.ku.dk).

Received 30 November 2016; accepted 8 January 2017; published online 27 February 2017; doi:10.1038/nm.4293

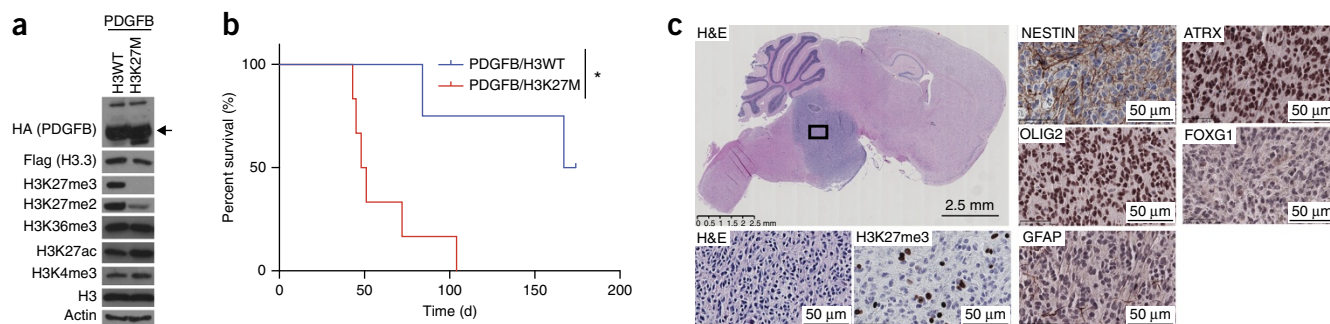


Figure 1 A mouse model of DIPG. (a) Cropped images of immunoblot showing exogenous expression of PDGFB, together with WT or K27M-mutated H3.3 in mouse NSCs. Immunoblot also shows the global loss of H3K27me3 and H3K27me2 levels in PDGFB/H3K27M NSCs. (b) Kaplan–Meier curve showing survival of mice injected into the pons with 10^4 PDGFB/H3WT ($n = 4$) or PDGFB/H3K27M ($n = 6$) NSCs. $*P = 0.0119$; log-rank test. (c) Immunohistochemistry of PDGFB/H3K27M tumor in mouse. H&E staining shows the localization of the tumor in the pons. The tumor shows strong staining for NESTIN/OLIG2/ATRX and weak staining for H3K27me3, FOXG1 and GFAP.

DIPGs^{14,16–18}. To better understand the role of the H3K27M protein in DIPGs, we sought to make a mouse model of DIPG. To that end, we expressed Flag-HA-tagged K27M H3.3 mutant in mouse *Trp53*^{−/−} neural stem cells (NSCs) or in NSCs expressing PDGFB. The expression of H3K27M to a level of 1% of total H3 (as determined by targeted mass spectrometry (MS)) led to a global reduction of H3K27me3 and H3K27me2, as determined by immunoblot and MS (Fig. 1a and Supplementary Fig. 1a). In agreement with a recent report¹⁹, *Trp53*^{−/−} NSCs expressing H3K27M did not develop tumors when injected into the mouse pons (Supplementary Fig. 1b,c). Co-expression of PDGFB and H3K27M resulted in marked improvement in the colony-forming ability of NSCs in soft agar (Supplementary Fig. 1d–f) and PDGFB/H3K27M NSCs formed tumors at a significantly faster rate than NSCs expressing PDGFB and wild-type H3 (PDGFB/H3WT) (Fig. 1b). Immunohistochemistry (IHC) of the brains of tumor-bearing mice confirmed the localization of tumors in the pons (Fig. 1c and Supplementary Fig. 1g). The tumours were positive for NESTIN and OLIG2 (which are the markers for progenitor cells and are often expressed in gliomas) and showed weak staining of GFAP (a marker for differentiated astrocyte) (Fig. 1c). Consistently with previous reports^{14,22}, tumours were ATRX positive and showed weak FOXG1 staining (Fig. 1c). PDGFB/H3K27M tumors showed reduced H3K27me3 levels as compared to PDGFB/H3WT tumors (Fig. 1c and Supplementary Fig. 1h). We also compared gene-expression profiles of mouse PDGFB/H3K27M tumors and human DIPGs. Hierarchical clustering of DIPGs (data obtained from three studies^{14,20,22}) using genes, which were previously shown to be differentially expressed in H3WT and H3K27M DIPGs²⁰, gave rise to two major clusters: cluster I, which contained primarily H3WT tumors, and cluster II or H3K27M-like cluster, which contained the majority of H3K27M tumors as well as a subgroup of H3WT tumors. Mouse H3K27M tumors clustered within cluster II, indicating that these tumors are similar to human H3K27M DIPGs (Supplementary Fig. 1i).

EZH2 activity is required for the growth of mouse DIPG cells *in vitro* and *in vivo*

Two recent studies showed that, despite the global reduction in H3K27me3 levels in H3K27M mutant tumor cells, several genes retained H3K27me3, and surprisingly, several loci, including some tumor-suppressor genes, even showed increased H3K27me3 enrichment^{20,21}. To test whether the remaining H3K27me3 present in H3K27M-positive DIPGs is required for tumor cell growth, we inhibited EZH2 activity in the mouse DIPG cellular model using two different inhibitors

(GSK343 and EPZ6438)^{7,23,24}. Both GSK343 and EPZ6438 are potent and highly selective EZH2 inhibitors, although EPZ6438 is more potent (Supplementary Fig. 2). As compared to DMSO treatment, the treatment of either PDGFB/H3WT or PDGFB/H3K27M NSCs with the EZH2 inhibitors led to reduction of cell proliferation and colony-forming activity (Fig. 2a and Supplementary Fig. 3a). Furthermore, EZH2-inhibitor-treated cells showed senescence-associated β -galactosidase (SA- β -gal) activity (Supplementary Fig. 3b), which suggests that such reduced proliferation is a result of increased senescence. These results demonstrate that the catalytic activity of PRC2 is required for the growth of mouse DIPG tumor cells *in vitro*.

To determine whether EZH2 is also required for tumor cell growth *in vivo*, we generated PDGFB/H3K27M NSCs in *Ezh2*^{fl/fl};CreER (*Ezh2*^{fl/fl}; PDGFB/H3K27M) background that allowed us to conditionally delete *Ezh2*. Treatment with 4-hydroxytamoxifen (4-OHT) led to a loss of EZH2 expression (Supplementary Fig. 4a), and, when injected into the mouse pons, the mice with the 4-OHT-treated cells showed significantly longer survival than the mice injected with control ethanol-treated cells ($P = 0.0088$; Supplementary Fig. 4b). To delete *Ezh2* in tumor cells *in vivo*, we injected *Ezh2*^{fl/fl};PDGFB/H3K27M NSCs in the mouse pons, and after 3 weeks, we treated the mice with tamoxifen. Tamoxifen-treated mice showed significantly longer survival than control oil-treated mice (Fig. 2b). Genotyping of a tumor isolated from one of the tamoxifen-treated mice showed that the tumor developed in tamoxifen-treated mice had escaped Cre-mediated deletion of the *Ezh2* gene (Supplementary Fig. 4c). Taken together, these results show that EZH2 is required for both the initiation of DIPG tumorigenesis and for the sustained growth of these tumors *in vivo*.

p16^{INK4A} (encoded by *INK4A* in the *CDKN2A* locus) is a tumor-suppressor protein that acts as a cell-cycle inhibitor, and its expression is strongly induced by stress and oncogene activation²⁵. One of the physiological functions of the polycomb group (PcG) proteins is to maintain low levels of *INK4A* expression, which is also a key mechanism by which increased levels or activity of the PcG proteins can contribute to tumorigenesis²⁵. Interestingly, we found that PDGFB/H3K27M NSCs showed higher H3K27me3 levels at the *Ink4a* promoter (Fig. 2c) and had reduced p16^{INK4A} expression when compared to PDGFB/H3WT NSCs (Fig. 2d). Treatment with the EZH2 inhibitors led to the reduction (for EPZ6438-treated cells, complete loss) in H3K27me3 levels at the *Ink4a* promoter and a corresponding dramatic increase in p16^{INK4A} levels (Fig. 2c,d). Similar results were obtained in PDGFB NSCs constitutively expressing H3.1K27M (Supplementary Fig. 4d–f), demonstrating that the regulation of

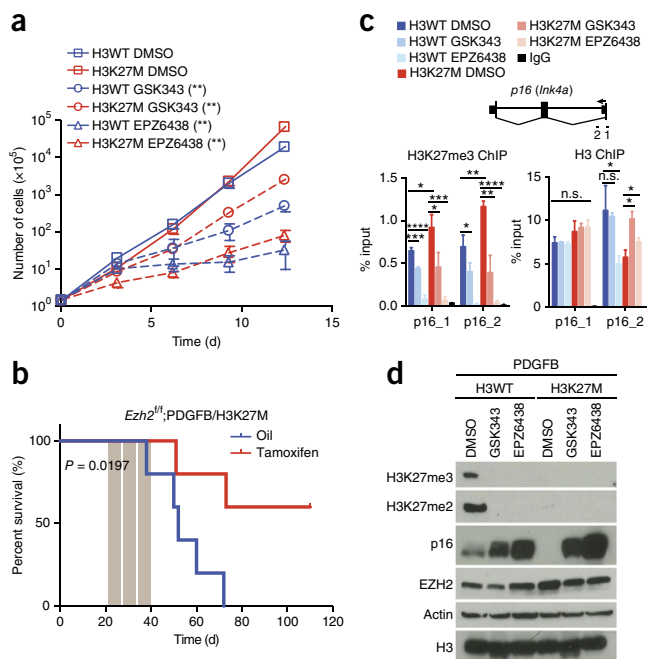


Figure 2 EZH2 inhibition affects the growth of H3K27M-positive mouse DIPG-like tumor cells *in vitro* and *in vivo*. **(a)** *In vitro* cell proliferation assay of PDGFB/H3WT and PDGFB/H3K27M NSCs upon treatment with two different EZH2 inhibitors (3- μ M concentration). Data are represented as mean \pm s.d.; $n = 3$ independent experiments. ** $P < 0.001$ (nonlinear regression). **(b)** Kaplan–Meier curve showing survival of mice with 10^4 *Ezh2*^{fl}/PDGFB/H3K27M NSCs and either oil ($n = 5$) or tamoxifen ($n = 5$). The treatment periods are indicated as three bars. Log-rank test was used to determine statistical significance. **(c)** ChIP analysis showing the enrichment of H3K27me3 over the *Ink4a* gene in DMSO-treated or EZH2-inhibitor-treated (3- μ M concentration; 12 d) NSCs. The mouse *Ink4a* gene and the location of the primers used for the analysis are also shown. Data are represented as mean \pm s.d.; $n = 3$ independent experiments. * $P < 0.05$, ** $P < 0.01$, *** $P < 0.001$, **** $P < 0.0001$, n.s., not significant; two-tailed unpaired Student's *t*-test. **(d)** Cropped images of immunoblots showing the H3K27me3 and H3K27me2 levels, as well as expression of p16^{INK4A}, in DMSO-treated or EZH2-inhibitor-treated (3 μ M; 12 d) of the indicated NSCs.

the *Ink4a* promoter is not dependent on the H3 mutant isoform. Interestingly, lower EZH2 inhibitor concentrations showed modest increase in p16^{INK4A} expression and a correspondingly milder effect on cell proliferation, demonstrating the strong correlation between the level of induced p16^{INK4A} expression and the extent of the effect on cell proliferation (Supplementary Fig. 4g,h). These results indicate that significant EZH2 activity remains locally at the *Ink4a* promoter in H3K27M cells, and that this activity is required for the repression of the *Ink4a* promoter and the maintenance of cell proliferation. Furthermore, the dependence on EZH2 activity makes the H3K27M cells susceptible to EZH2 inhibitors, which cause derepression of p16^{INK4A} and growth arrest.

EZH2 inhibition affects the proliferation of patient-derived DIPG cell lines

To investigate the relevance of these results for human DIPGs, we tested the effect of EZH2-inhibitor treatment on six primary human DIPG cell lines (DIPG007, DIPG012, SF7761, SF8628, DIPG017 and DIPG018) and one pediatric glioblastoma multiforme (GBM) cell line (GBM003) expressing H3K27M, one pediatric GBM cell line with G34R mutation

in H3.3 (GBM002) and one pediatric GBM with wild-type H3 (SF188) (Fig. 3 and Supplementary Fig. 5a,b). All the H3K27M mutant cell lines except DIPG018 harbored a mutation in *H3F3A* (H3.3), whereas DIPG018 harbored a mutation in *HIST1H3B* (H3.1). All the H3K27M-mutant cell lines tested showed reduced proliferation in response to EZH2-inhibitor treatment (Fig. 3b–e and Supplementary Fig. 5c), and this effect was associated with decreased H3K27me3 enrichment on the *INK4A* promoter and a corresponding increase in p16^{INK4A} expression (Fig. 3g–i and Supplementary Fig. 5d–g). In contrast to the H3K27M cell lines, the proliferation of the pediatric GBM cell lines with WT or G34R-mutant H3 (SF188 and GBM002) was not affected by EZH2-inhibitor treatment (Fig. 3f and Supplementary Fig. 5c). Accordingly, EZH2 inhibition did not affect colony formation of SF188, whereas DIPG012 and SF8628 formed considerably fewer colonies upon EZH2-inhibitor treatment (Supplementary Fig. 3a). Consistently, EZH2-inhibitor treatment led to increased SA- β -gal activity in the DIPG cell lines (Supplementary Fig. 3b). Cell-cycle analysis of EZH2-inhibitor-treated DIPG cells showed considerably fewer cells in S phase with a corresponding increase in number of cells in G1 phase, whereas EZH2-inhibitor treatment did not affect the cell-cycle profile of SF188 (Supplementary Fig. 3c). These results demonstrate that human DIPG cells, similarly to the mouse DIPG cells, become senescent in response to EZH2 inhibition.

Effect of EZH2 inhibition on tumor cell proliferation is dependent on functional p16^{INK4A}

The observation that DIPG cells undergo senescence in response to EZH2 inhibition, and that this correlates with an increase in p16^{INK4A} expression, suggests that p16^{INK4A} could be causally involved in response to EZH2 inhibition. Cell lines such as SF188 or NSCs with *Trp53* knockdown or knockout express high levels of p16^{INK4A}, with no negative effect on cell proliferation; this indicates that the p16^{INK4A} pathway is nonfunctional (Figs. 3a and 4a,c). These cells are insensitive to EZH2 inhibition (Fig. 3f and 4b,d), which suggests that the sensitivity of tumor cells to EZH2 inhibition is dependent on a functional p16 pathway. Furthermore, EZH2 inhibition failed to induce p16^{INK4A} in GBM002 cells, and thus these cells were not affected by EZH2 inhibition (Supplementary Fig. 5c,e). To directly test the involvement of p16^{INK4A} in determining the sensitivity of DIPGs to EZH2 inhibition, we generated DIPG007 p16^{INK4A}-knockout cells (Fig. 4e and Supplementary Fig. 5h). As shown in Figure 4f, these cells are insensitive to EZH2 inhibition. Additionally, the induced expression of p16^{INK4A} in DIPG007 was sufficient to induce growth arrest (Fig. 4g,h). These results strongly suggest that the effect of EZH2 inhibitors on DIPG tumor cells is mediated by induced p16^{INK4A} expression, and that it is the p16^{INK4A} status that determines the sensitivity of tumor cells to EZH2 inhibition.

Interestingly, although all the DIPG cell lines tested were sensitive to EZH2 inhibition, two of them expressed high p53 levels and correspondingly low p21 expression, which suggests that the *TP53* gene is mutated in these cells (Supplementary Fig. 5i,j). Thus, we determined the mutation status of *TP53* in SF188 and the four DIPG cell lines. As expected, DIPG007 and SF7761 cells did not have any deleterious mutations, whereas SF188, DIPG012 and SF8628 had at least one deleterious *TP53* mutation²⁶ (Supplementary Table 1). Interestingly, unlike SF188, DIPG cell lines harboring *TP53* mutations did not show high p16^{INK4A} expression and were sensitive to EZH2 inhibition (Fig. 3c,e). These results indicate that p16^{INK4A} is repressed by PRC2 in H3K27M DIPGs, even in the presence of *TP53* mutation. To investigate this further, we analyzed the status of the p16^{INK4A} and

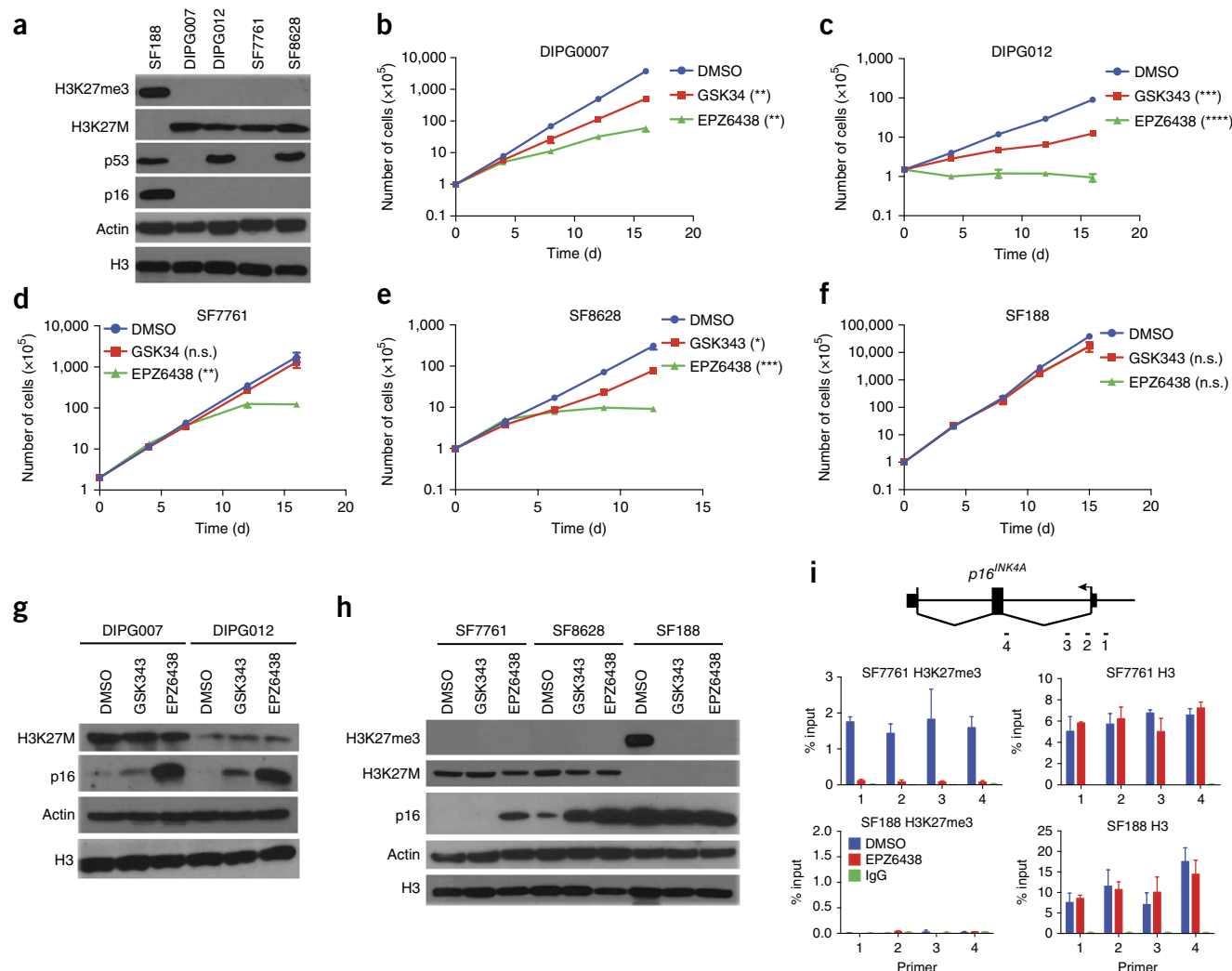


Figure 3 EZH2 inhibition affects the growth of primary H3K27M-positive human DIPG cells. **(a)** Cropped images of immunoblots showing H3K27me3, H3K27M, p16^{INK4A} and p53 levels in five pediatric glioma cell lines. **(b–f)** *In vitro* cell-proliferation assays of four primary DIPG cell lines (DIPG007 **(b)**, DIPG012 **(c)**, SF7761 **(d)** and SF8628 **(e)**) and one pediatric GBM cell line (SF188 **(f)**) upon treatment with two different EZH2 inhibitors (3 μ M). Data are represented as mean \pm s.d.; $n = 3$ independent experiments. * $P < 0.05$, ** $P < 0.01$, *** $P < 0.001$, **** $P < 0.0001$, n.s., not significant (nonlinear regression). **(g,h)** Cropped images of immunoblots showing H3K27me3 and p16^{INK4A} levels in DMSO-treated or EZH2-inhibitor-treated glioma cell lines. **(i)** ChIP analysis showing the enrichment of H3K27me3 over the *INK4A* gene in SF7761 and SF188 cells upon DMSO or EZH2-inhibitor treatment (3 μ M; 12 d). Data are represented as mean \pm s.d.; $n = 3$. The human *INK4A* gene and the location of the primers used for the analysis are also shown.

p53 proteins and genes in a cohort of tumor samples isolated from DIPG ($n = 19$) and pediatric GBM ($n = 22$) patients. All except one DIPG tumor carried a mutation in either *H3F3A* (H3.3) or *HIST1H3B* (H3.1), leading to the expression of H3K27M (**Supplementary Fig. 6a**). Consistently with this, all DIPGs showed a global decrease of H3K27me3 levels, as analyzed by IHC. The majority of pediatric GBMs were H3K27me3 positive, whereas few pediatric GBMs had H3K27M mutation and were H3K27me3 negative. Around 66% of all the tumors showed positive p53 staining in IHCs, suggesting that these tumors harbor a mutation in *TP53*, which was confirmed by sequencing in a subset of the tumors. Interestingly, the majority of tumors (32/44) were p16^{INK4A} negative and had no correlation with pathology (DIPG/GBM) or *TP53* mutation (**Supplementary Fig. 6a**). To test whether low p16^{INK4A} expression is associated with deletion of the *CDKN2A* locus, we analyzed the integrity of the *CDKN2A* locus by either cytoscanner analysis or fluorescence *in situ* hybridization (FISH) in a subset of tumors. *CDKN2A* deletion is rare in

DIPGs²⁷ and, consistently with this, the *CDKN2A* locus was found to be intact in the majority of the analyzed tumors (**Supplementary Fig. 6a**). Furthermore, analysis of DNA methylation data from a published report²² showed very low DNA methylation over the *CDKN2A* locus in H3K27M DIPGs (**Supplementary Fig. 6b**). Taken together, these data show that in the majority of DIPGs, p16^{INK4A} is repressed regardless of *TP53* mutations, which is in contrast to the observation in adult GBMs that *TP53* mutation is often associated with high p16^{INK4A} expression²⁸. Furthermore, the lack of p16^{INK4A} expression in DIPGs is not a result of genomic deletion of the locus and most likely not due to DNA methylation, but due instead to PRC2-mediated transcriptional repression, which is supported by our observation in DIPG cell lines (see further below).

To test whether the p16^{INK4A} status also predicts the response to EZH2 inhibition in adult gliomas, we used mouse models representing two different GBM subtypes. *Trp53*^{−/−} NSCs expressing PDGFβ represent the proneural subtype, whereas *Ink4a*^{−/−}/*Arf*^{−/−} NSCs expressing

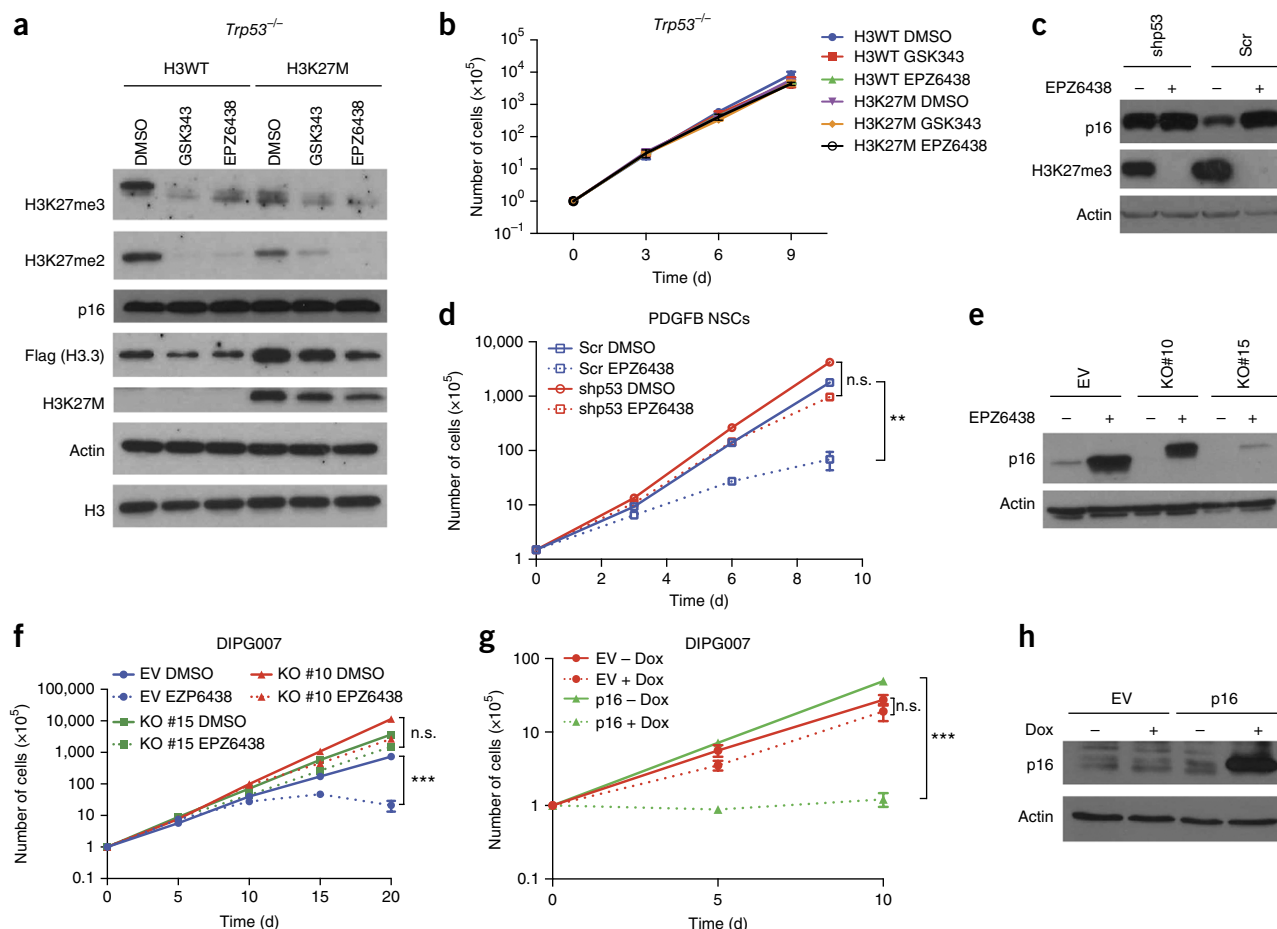


Figure 4 Effect of EZH2 inhibition on cell proliferation is dependent on functional p16^{INK4A}. **(a)** Cropped images of immunoblots for the indicated proteins in DMSO-treated or EZH2-inhibitor-treated (3 μ M; 9 d) *Trp53*^{-/-};H3WT NSCs or *Trp53*^{-/-};H3K27M NSCs. **(b)** Cell-proliferation assay of *Trp53*^{-/-} NSCs expressing WT or K27M-mutated H3.3 upon treatment with DMSO or EZH2 inhibitors (3 μ M). Data are represented as mean \pm s.d.; $n = 3$ independent experiments. **(c)** *In vitro* cell-proliferation assay in p53-knockdown PDGFB NSCs upon treatment with EPZ6438 (3 μ M). Data are represented as mean \pm s.d.; $n = 3$ independent experiments. ** $P < 0.01$, n.s., not significant; nonlinear regression. **(d)** Cropped images of immunoblots of lysates prepared from the cells at day 9 shown in **c**. **(e)** Cropped images of immunoblots showing expression of p16^{INK4A} in two DIPG007 p16^{INK4A} knockout clones (KO #10 and KO #15). Asterisk indicates the position of predicted p16^{INK4A}/p14^{ARF} hybrid protein. **(f)** *In vitro* cell-proliferation assay in control (empty vector, EV) and two DIPG007 clones in which p16^{INK4A} was deleted by CRISPR. **(g)** *In vitro* proliferation assay in DIPG007 cells upon inducible expression of p16^{INK4A}. DIPG007 cells were transfected with EV or p16^{INK4A}-inducible expression vector. p16^{INK4A} expression was induced by doxycycline (Dox) treatment. **(h)** Cropped images of immunoblots of lysates prepared from the cells at day 10 shown in **g**. For all proliferation assays, data are represented as mean \pm s.d.; $n = 3$. ** $P < 0.01$, *** $P < 0.001$, n.s., not significant; nonlinear regression.

constitutive active epidermal growth-factor receptor (*EGFR) represent the classical subtype²⁸. Treatment of these NSCs with EZH2 inhibitors did not affect their proliferation (**Supplementary Fig. 7a–c**). These results are consistent with our observations in pediatric gliomas.

We also tested how EZH2 inhibition would affect the proliferation of four patient-derived primary glioma neural stem (GNS) cell lines²⁹. Out of four GNS cell lines tested, one had an *INK4A* deletion (G14), whereas the others showed high p53 and p16^{INK4A} levels, suggesting mutation in *TP53* and nonfunctional p16^{INK4A} status (**Supplementary Fig. 7d**). None of the four GNS cell lines was affected by EZH2-inhibitor treatment (**Supplementary Fig. 7e,f**), suggesting that, as in pediatric gliomas, adult gliomas expressing high levels of p16^{INK4A} are not sensitive to EZH2 inhibitors.

Strong polycomb targets retain H3K27me3 in H3K27M-expressing cells

To obtain insights into the potential mechanism by which H3K27M affects H3K27me3 distribution in NSCs and how it can contribute to

the development of DIPGs, we mapped the genome-wide distribution of H3K27me3 by ChIP, and followed this with high-throughput sequencing (ChIP-seq), in PDGFB/H3WT and PDGFB/H3K27M NSCs. Given that H3K27M cells show global loss of H3K27me3, conventional reads per million (r.p.m.) ChIP-seq normalization would lead to overestimation of H3K27me3 in H3K27M cells. Thus, we developed a new computational method to normalize ChIP-seq data, which is based on estimation of background read density (BRD) in different samples (**Supplementary Fig. 8a**, Leblanc *et al.*, unpublished results). Normalization factors calculated by BRD method were comparable to the factors calculated by ChIP-Rx normalization, which is based on spike-in with exogenous reference genome³⁰ (B.L, F.M. and K.H., unpublished results).

When we compared them to PDGFB/H3WT NSCs, we found loci that showed reduced, unchanged or increased H3K27me3 in PDGFB/H3K27M NSCs (**Fig. 5a**). Consistent with the ChIP-qPCR analysis (**Fig. 2c**), the *Cdkn2a* locus showed increased H3K27me3 enrichment in PDGFB/H3K27M NSCs, whereas treatment with

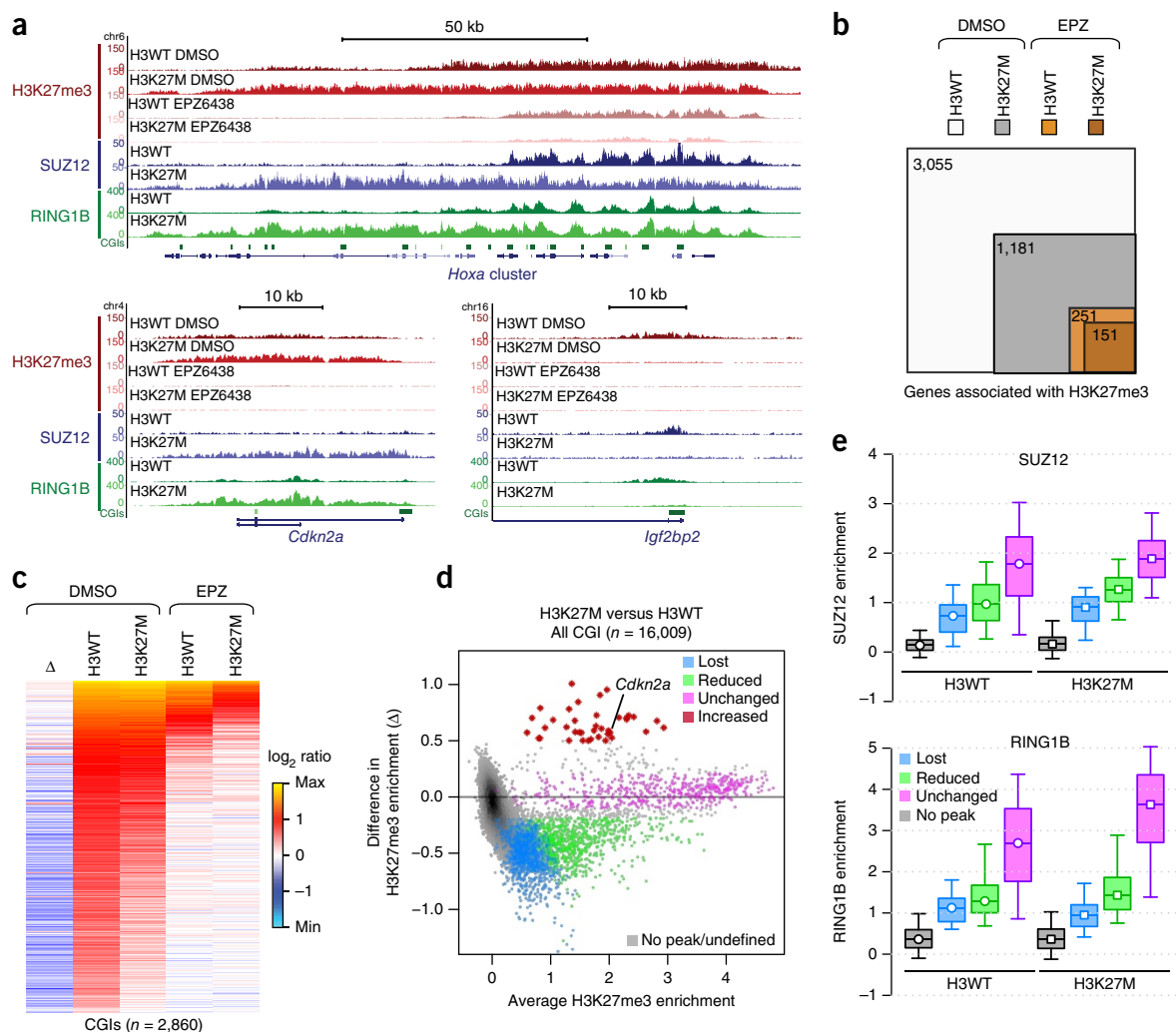


Figure 5 Genome-wide effects of H3K27M at CGIs are linked to H3K27me3, SUZ12 and RING1B enrichment in H3WT. (a) Examples of tracks showing H3K27me3, SUZ12 and RING1B enrichment in PDGFB/H3WT and PDGFB/H3K27M NSCs. Loci shown here are the *Hoxa* cluster, *Cdkn2a* and *Igf2bp2*. (b) Overlap between sets of genes associated with H3K27me3 in DMSO (gray) or EPZ6438 (“EPZ,” gold)-treated PDGFB/H3WT and PDGFB/H3K27M NSCs. Box and overlap areas are indicative of the size of each gene set. (c) Heat map representing the \log_2 ratio of H3K27me3 over IgG ChIP-seq enrichments on CGIs in untreated and treated cells (columns 2–5 from the left). First column shows the difference (Δ) in H3K27me3 enrichment in H3K27M versus H3WT cells (both untreated). (d) Mean-difference representation of H3K27me3-enrichment variations on CGIs in H3K27M versus H3WT cells. In relation to c, the x axis corresponds to the average of columns 2 and 3; the y axis corresponds to the first column. H3K27me3 variations on CGIs were categorized as lost ($n = 1,230$), reduced ($n = 817$), unchanged ($n = 521$) or increased ($n = 39$), shown, respectively, in blue, green, pink-purple and red on the mean-difference plot. CGIs that are not associated with H3K27me3 ($n = 13,147$) or that were left undefined ($n = 255$) are shown in gray. (e) Box plots showing SUZ12 (top) and RING1B (bottom) enrichment at CGIs corresponding to different categories in H3WT and H3K27M cells.

EPZ6438 resulted in a dramatic decrease of H3K27me3 (Fig. 5a). As compared to H3WT NSCs, more than half of the genes lost H3K27me3 in H3K27M NSCs, whereas the majority of the genes lost H3K27me3 upon treatment with EPZ6438 (Fig. 4b). The fact that there was nearly complete overlap between sets of H3K27me3-associated genes in PDGFB/H3WT and PDGFB/H3K27M NSCs suggests that there were few *de novo* polycomb targets in PDGFB/H3K27M NSCs (Fig. 5b).

The majority of H3K27me3-positive genes were associated with CpG islands (CGIs) (Supplementary Fig. 8b), and in H3WT NSCs, genes that are not associated with CGIs had significantly lower H3K27me3 enrichment than CGI-associated genes (Supplementary Fig. 8c). Moreover, given that polycomb complexes are known to target CGIs³¹, we focused detailed differential analyses of H3K27me3 enrichment on these elements, applying the data-normalization

scheme shown in Supplementary Figure 8a. Heat-map representation of H3K27me3 illustrates that the CGIs with higher H3K27me3 enrichment in H3WT tend to remain associated with H3K27me3 in H3K27M NSCs (Fig. 5c). Furthermore, CGIs with the highest H3K27me3 levels in untreated NSCs remain associated with H3K27me3 even in EPZ6438-treated NSCs (Fig. 5c), which suggests that ‘strong’ polycomb target genes—which are perhaps essential for defining the cell type—are more likely to resist the inhibitory effect of H3K27M or EZH2 inhibitors (see further below).

We categorized H3K27me3-associated CGIs in H3WT NSCs into four groups: “lost,” “reduced,” “unchanged” and “increased,” according to the effect on H3K27me3 enrichment over CGIs in H3K27M NSCs (Fig. 5d and Supplementary Fig. 8d). As also shown on the heat-map representation, CGIs in the “lost” group showed the lowest H3K27me3 enrichment, whereas “reduced” CGIs showed higher,

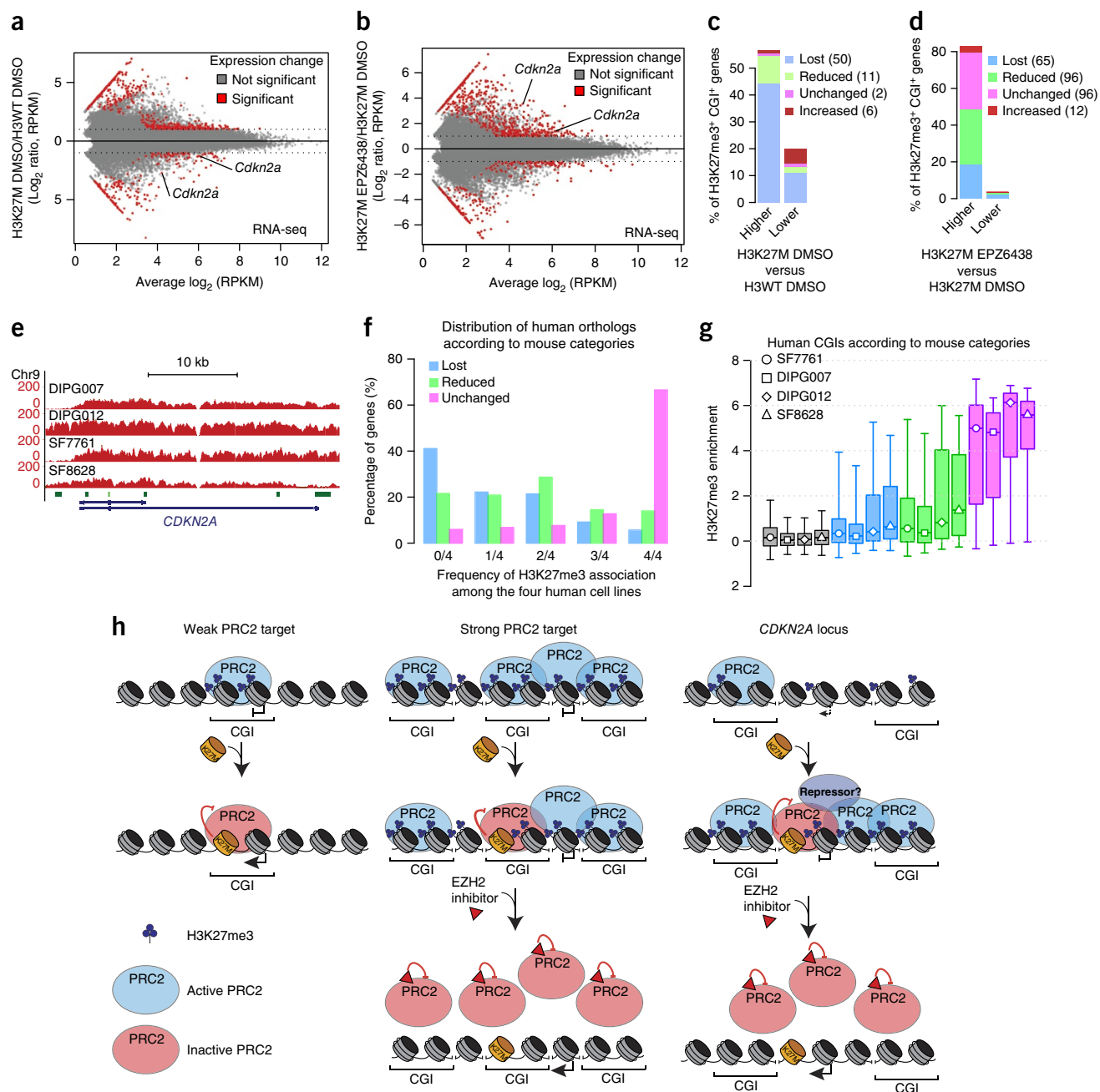


Figure 6 H3K27M and EZH2 inhibition leads to significant gene-expression changes. **(a)** Scatter plot showing gene-expression changes in H3K27M cells as compared to H3WT cells. **(b)** Same as in **a**, but comparing expression in EPZ6438-treated and DMSO-treated H3K27M cells. **(c)** Percentage of differentially expressed H3K27me3 and CGI-associated genes shown in **a** that belong to different categories. **(d)** Same as in **c**, but for differentially expressed genes shown in **b**. **(e)** H3K27me3 ChIP-seq tracks showing enrichment over *CDKN2A* locus in four DIPG cell lines. **(f)** Histogram showing the frequency of H3K27me3 association among the four human DIPG cell lines for human orthologs of mouse genes corresponding to lost, down or unchanged categories. **(g)** Boxplot representing H3K27me3 enrichment in human DIPG cell lines for human CGIs associated with the three sets of orthologous genes shown in **f**. Boxes span second and third quartiles, and center indicates the median of the distribution. Whiskers indicate 5th and 95th percentiles. **(h)** A working model for the locus-specific effects of H3K27M (see Discussion for details).

and “unchanged” CGIs highest, H3K27me3 enrichment (**Fig. 5d** and **Supplementary Fig. 8e**). The CGIs with “increased” H3K27me3 levels constituted a distinct group of few CGIs that showed no correlation with H3K27me3 levels in the PDGFB/H3WT NSCs, which suggests that this group of CGIs is regulated differently than other CGIs in the H3K27M-expressing cells (**Fig. 5d**). Consistently, most of the genes that were not associated with CGI and had lower

H3K27me3 enrichment in H3WT NSCs either lost or showed reduced H3K27me3 in H3K27M NSCs (**Supplementary Fig. 8f**). These results were confirmed by an independent H3K27me3 ChIP-seq analysis (**Supplementary Fig. 8g–i**).

We also analyzed the genome-wide location of SUZ12 and RING1B, which are core components of PRC2 and PRC1, respectively, in PDGFB/H3WT and PDGFB/H3K27M NSCs. Consistent with

H3K27me3 enrichment analysis, CGIs in the “lost” and “reduced” categories showed low PRC2/PRC1 enrichment, whereas CGIs in the “unchanged” category showed high enrichment both in H3WT cells and H3K27M cells (Fig. 5e and Supplementary Fig. 8j,k). The majority of CGIs in the “increased” category showed increased enrichment of both SUZ12 and RING1B, whereas a modest increase in only RING1B enrichment was observed in “unchanged” CGIs (Supplementary Fig. 8j,k). We validated the effect of H3K27M on H3K27me3/SUZ12/RING1B enrichment over a few genes from each of the four groups by ChIP-qPCR (Supplementary Fig. 8l). We also determined the chromatin distribution of H3WT and H3K27M histones over these genes by performing ChIP using Flag-antibody, but did not find strong evidence for the preferential distribution of WT or mutant histones (Supplementary Fig. 8l).

To determine whether any distinct features were associated with “unchanged” CGIs, we measured the distance between adjacent CGIs and categorized them as isolated (one CGI within 30 kb) or clustered (more than one CGI within 30 kb) (Supplementary Fig. 9a). Interestingly, ~90% of CGIs in the “unchanged” category were clustered (Supplementary Fig. 9b). Moreover, isolated CGIs in the “unchanged” category tend to be longer than the isolated CGIs in “lost” and “reduced” categories (Supplementary Fig. 9c). These data suggest that the strong polycomb targets have either clustered or longer CGIs. However, the fact that a substantial number of “lost” and “reduced” CGIs are also clustered suggests that being in a cluster is required, but not sufficient, for retaining H3K27me3 in the presence of H3K27M.

H3K27M leads to significant gene-expression changes

To identify the changes in gene expression associated with alterations in H3K27me3 enrichment, we performed RNA-seq in DMSO or EPZ6438-treated H3WT and H3K27M NSCs. The majority of differentially expressed genes in H3K27M NSCs was not associated with H3K27me3 in H3WT NSCs, suggesting an indirect effect (Supplementary Fig. 9d). Consistent with the protein levels (Fig. 2d), *Cdkn2a* was one of the most repressed genes in H3K27M NSCs, whereas it was strongly activated in EPZ6438-treated cells (Fig. 6a,b). As compared to H3WT NSCs, H3K27M NSCs did not show any change in expression of the genes in the “unchanged” category, whereas a subset of genes in the “lost” and “reduced” categories showed higher expression in H3K27M NSCs (Fig. 6c). Besides *Cdkn2a*, there were four *Hox* genes (*Hoxa3–Hoxa6*), which belonged to the “increased” category and showed reduced expression in H3K27M NSCs (Fig. 6c and Supplementary Table 2). Furthermore, consistent with the near-complete loss of H3K27me3 upon EPZ6438 treatment, most of the differentially expressed H3K27me3/CGI-associated genes that included genes in the “unchanged” and “increased” categories showed higher expression in EPZ6438-treated H3K27M NSCs (Fig. 6d).

H3K27me3-enriched loci are retained in human DIPG cells

To understand whether H3K27M-expressing human tumors would have a distribution of H3K27me3 similar to that observed in mouse NSCs expressing H3K27M, we mapped the distribution of H3K27me3 genome wide in the four primary H3K27M-mutant DIPG cell lines. Despite the global decrease of H3K27me3 (Fig. 3a), all four cell lines showed a substantial amount of gene-specific H3K27me3 enrichment. Consistent with the ChIP-qPCR analysis, *CDKN2A* showed strong H3K27me3 enrichment in all four DIPG cell lines (Fig. 6e). To compare H3K27me3 distribution in human DIPG cell lines with that of mouse DIPG cells, we identified the human orthologs of the

mouse genes associated with CGIs corresponding to one of the three categories: “lost,” “reduced” or “unchanged” (Supplementary Fig. 9f). The orthologs of most of the genes associated with “unchanged” CGIs showed H3K27me3 enrichment in all four DIPG cell lines, whereas orthologs of most of the genes associated with “lost” CGIs showed no H3K27me3 enrichment in any of the DIPG cell lines (Fig. 6f). These results demonstrate a substantial overlap between genes that retain H3K27me3 in mouse and human primary DIPGs expressing H3K27M, and provide further validation of the PDGFB/H3K27M NSCs as a model for human DIPG.

Next, for each DIPG cell line, we calculated the H3K27me3 enrichment over the CGIs associated with the human orthologs corresponding to individual categories (Supplementary Fig. 9f). Consistent with the mouse data, the human orthologs of the “lost” CGIs had the least H3K27me3 enrichment, whereas orthologs of “reduced” CGIs had higher, and orthologs of “unchanged” CGIs highest, H3K27me3 enrichment (Fig. 6g).

DISCUSSION

We have used a combination of mouse modeling and the analysis of primary human DIPGs to understand the role of H3K27M in the induction and maintenance of tumorigenesis. In agreement with previous findings, we show that H3K27me3 is retained at several loci in H3K27M mutant DIPGs, we provide insights into the mechanism by which H3K27me3 is retained at specific loci and we demonstrate that DIPGs are dependent on PRC2 for the proliferation. Overexpression of PDGFB, which is a strong mitogenic factor that binds to both PDGF receptors (PDGFRA and PDGFRB), has been used previously in several studies to model gliomas in mice³². As in adult gliomas, it is the increased levels of PDGFRA and not PDGFB, that leads to increased PDGF signaling in DIPGs, and thus, the use of PDGFB overexpression in our mouse model does not strictly reflect the genetic changes in DIPGs. However, we have extensively validated the findings obtained using the mouse model in human primary DIPG cell lines and therefore also validated the use of the model for the study of human DIPGs.

Our genomic analyses show that H3WT-expressing cells contain weak polycomb targets, characterized by isolated or short CGIs and low PRC2/H3K27me3 enrichment and strong polycomb targets, characterized by clustered or long CGIs and high PRC2/H3K27me3 enrichment (Fig. 6h). In tumor cells, H3K27M constitutes a minor part of total H3 and uniformly incorporates in the chromatin at low levels. The incorporation of H3K27M at weak polycomb targets completely inhibits the already limited PRC2 activity that leads to loss of H3K27me3. Because strong polycomb targets have potentially more PRC2 binding sites than weak targets, the incorporation of H3K27M at these loci would not be sufficient to reduce the overall PRC2 activity, and H3K27me3 levels thus remain unaffected. Few loci, exemplified by *CDKN2A*, show increased H3K27me3 enrichment in H3K27M cells. *CDKN2A* shows low PRC2/H3K27me3 enrichment in H3WT cells associated with low p16^{INK4A} expression. In H3K27M cells, *INK4A* levels are further decreased, through a so-far unknown mechanism that may involve the selection of a subpopulation of cells that becomes transformed (see further below) and/or the transcriptional repression by a protein that leads to increased PRC2 recruitment and thus increased H3K27me3 enrichment at *INK4A* (Fig. 6h).

Gene ontology (GO) analysis of genes associated with unchanged CGIs showed substantial enrichment of classical polycomb target genes that are involved in the regulation of transcription during development, pattern specification and embryonic development (see

Supplementary Table 3 for the list of GO terms). The role of these genes in regulating cell fate, in combination with the fact that they remain H3K27me3 positive in H3K27M-expressing cells, indicates that the repression of these genes is required to maintain the cellular identity of DIPGs. In addition to these genes, 20 genes acquired higher levels of H3K27me3 in PDGFB/H3K27M NSCs as compared to PDGFB/H3WT NSCs (**Supplementary Table 2**). This is a distinct set of genes that does not have high levels of H3K27me3 in H3WT-expressing cells, and they seem to be selected for during the transformation process. Prominent among these is the tumor-suppressor locus *Cdkn2a*. Other genes include genes encoding the homeobox proteins HOXA1–HOXA6, and transcription factors regulating neurogenesis, such as those encoding OTX2, IRX3, IRX5, ZIC1, ZIC4 and TBX2. On the basis of the identity of these genes, it is tempting to speculate that H3K27M expression leads to the selection of a cell type during the transformation process in which these genes are silenced by the PcG proteins. Furthermore, the fact that H3K27M expression does not lead to the accumulation of H3K27me3 on novel genes suggests that the main effect of H3K27M is to reinforce a transcriptional pattern specific for the cell-of-origin of DIPGs, as has been also proposed by others (see for example, ref. 33).

Another striking result is the fact that all the H3K27M-expressing cells that we have analyzed retained H3K27me3 on the *CDKN2A* locus. This locus serves as an important fail-safe mechanism that helps to protect cells from oncogene-induced transformation, and the silencing of this locus might be an important event in the genesis of DIPGs. Consistent with this notion, we found that the sensitivity of tumor cells for EZH2 inhibitors is dependent on the presence of p16^{INK4A}. Given that our analyses of primary tumors show that the *CDKN2A* locus is intact and that p16^{INK4A} is not expressed, likely owing to polycomb-mediated repression, we propose that EZH2 inhibitors could be suitable anti-DIPG agents. Pharmacologic inhibition of EZH2 has been shown to affect the proliferation and survival of other tumors, including lymphomas expressing hyperactive EZH2 mutants^{6–8} and malignant rhabdoid tumors²⁴. EPZ6438 and other EZH2 inhibitors are currently in phase 1/2 clinical trials in patients with lymphoma and rhabdoid tumors. Although the currently tested available EZH2 inhibitors have all been shown to interact with the two drug efflux transporters ABCB1 and/or ABCG2, and therefore show restricted brain penetration, EPZ6438 penetration was increased by the ABCB1/ABCG1 inhibitor elacridar³⁴. Thus, EPZ6438 might be a suitable candidate for further preclinical validation of EZH2 as a target for the treatment of patients with DIPG.

METHODS

Methods, including statements of data availability and any associated accession codes and references, are available in the [online version of the paper](#).

Note: Any Supplementary Information and Source Data files are available in the online version of the paper.

ACKNOWLEDGMENTS

We thank members of the Helin laboratory for discussions. F.M. was supported by a postdoctoral fellowship from EMBO (874-2011). D.P. was supported by a postdoctoral fellowship from EMBO (1411-2011) and the Danish Medical Research Council. I.C. was supported by a fellowship from the Lundbeck Foundation. The work in the Helin laboratory was supported by the Danish Medical Research Council (DFF – 4004-00081), the Danish National Research Foundation (DNRF 82), and through a center grant from the Novo Nordisk Foundation (The Novo Nordisk Foundation Section for Stem Cell Biology

in Human Disease). A.M.C. acknowledges support from the Xarxa de Bancs de Tumors de Catalunya (XBTC) sponsored by Pla Director d'Oncologia de Catalunya, and funding from the Fondo Alicia Pueyo, AECC Scientific Foundation, European Union Seventh Framework Programme (FP7/2007-2013) under Marie Curie International Reintegration Grant (PIRG-08-GA-2010-276998) and ISCIII-FEDER (CP13/00189). We thank S. Pollard for the gift of GNS cell lines, N. Gupta for providing the SF7761 and SF8628 cell lines and L. Uhrbom and P. Lewis for plasmids.

AUTHOR CONTRIBUTIONS

F.M. performed the majority of the experiments; S.W., D.P.P., J.W.H., C.Z. and I.C. performed the remaining experiments. The bioinformatics analyses were performed by B.L. and J.V.J.; N.R. and B.T.P. contributed to gene-expression analysis. A.T. and O.N.J. performed MS analysis. N.G.O., C.L., M.S., C.d.T., J.M. and A.M.C. analyzed the primary tumor samples. A.M.C. provided DIPG cell lines. F.M. and K.H. prepared the manuscript. All authors discussed the results and commented on the manuscript.

COMPETING FINANCIAL INTERESTS

The authors declare no competing financial interests.

Reprints and permissions information is available online at <http://www.nature.com/reprints/index.html>.

- Varambally, S. *et al.* The polycomb group protein EZH2 is involved in progression of prostate cancer. *Nature* **419**, 624–629 (2002).
- Helin, K. & Dhanak, D. Chromatin proteins and modifications as drug targets. *Nature* **502**, 480–488 (2013).
- Morin, R.D. *et al.* Frequent mutation of histone-modifying genes in non-Hodgkin lymphoma. *Nature* **476**, 298–303 (2011).
- Morin, R.D. *et al.* Somatic mutations altering EZH2 (Tyr641) in follicular and diffuse large B-cell lymphomas of germinal-center origin. *Nat. Genet.* **42**, 181–185 (2010).
- Pasqualucci, L. *et al.* Analysis of the coding genome of diffuse large B-cell lymphoma. *Nat. Genet.* **43**, 830–837 (2011).
- Knutson, S.K. *et al.* A selective inhibitor of EZH2 blocks H3K27 methylation and kills mutant lymphoma cells. *Nat. Chem. Biol.* **8**, 890–896 (2012).
- Knutson, S.K. *et al.* Selective inhibition of EZH2 by EPZ-6438 leads to potent antitumor activity in EZH2-mutant non-Hodgkin lymphoma. *Mol. Cancer Ther.* **13**, 842–854 (2014).
- McCabe, M.T. *et al.* EZH2 inhibition as a therapeutic strategy for lymphoma with EZH2-activating mutations. *Nature* **492**, 108–112 (2012).
- Konze, K.D. *et al.* An orally bioavailable chemical probe of the Lysine Methyltransferases EZH2 and EZH1. *ACS Chem. Biol.* **8**, 1324–1334 (2013).
- Ernst, T. *et al.* Inactivating mutations of the histone methyltransferase gene EZH2 in myeloid disorders. *Nat. Genet.* **42**, 722–726 (2010).
- Ntziachristos, P. *et al.* Genetic inactivation of the polycomb repressive complex 2 in T cell acute lymphoblastic leukemia. *Nat. Med.* **18**, 298–301 (2012).
- Hargrave, D., Bartels, U. & Bouffet, E. Diffuse brainstem glioma in children: critical review of clinical trials. *Lancet Oncol.* **7**, 241–248 (2006).
- Laigle-Donadey, F., Doz, F. & Delattre, J.-Y. Brainstem gliomas in children and adults. *Curr. Opin. Oncol.* **20**, 662–667 (2008).
- Schwartzentruber, J. *et al.* Driver mutations in histone H3.3 and chromatin remodelling genes in paediatric glioblastoma. *Nature* **482**, 226–231 (2012).
- Wu, G. *et al.* Somatic histone H3 alterations in pediatric diffuse intrinsic pontine gliomas and non-brainstem glioblastomas. *Nat. Genet.* **44**, 251–253 (2012).
- Buczkowicz, P. *et al.* Genomic analysis of diffuse intrinsic pontine gliomas identifies three molecular subgroups and recurrent activating ACVR1 mutations. *Nat. Genet.* **46**, 451–456 (2014).
- Taylor, K.R. *et al.* Recurrent activating ACVR1 mutations in diffuse intrinsic pontine glioma. *Nat. Genet.* **46**, 457–461 (2014).
- Fontebasso, A.M. *et al.* Recurrent somatic mutations in ACVR1 in pediatric midline high-grade astrocytoma. *Nat. Genet.* **46**, 462–466 (2014).
- Lewis, P.W. *et al.* Inhibition of PRC2 activity by a gain-of-function H3 H3 mutation found in pediatric glioblastoma. *Science* **340**, 857–861 (2013).
- Bender, S. *et al.* Reduced H3K27me3 and DNA hypomethylation are major drivers of gene expression in K27M mutant pediatric high-grade gliomas. *Cancer Cell* **24**, 660–672 (2013).
- Chan, K.-M. *et al.* The histone H3.3K27M mutation in pediatric glioma reprograms H3K27 methylation and gene expression. *Genes Dev.* **27**, 985–990 (2013).
- Sturm, D. *et al.* Hotspot mutations in H3F3A and IDH1 define distinct epigenetic and biological subgroups of glioblastoma. *Cancer Cell* **22**, 425–437 (2012).
- Verma, S.K. *et al.* Identification of potent, selective, cell-active inhibitors of the histone lysine methyltransferase EZH2. *ACS Med. Chem. Lett.* **3**, 1091–1096 (2012).

24. Knutson, S.K. *et al.* Durable tumor regression in genetically altered malignant rhabdoid tumors by inhibition of methyltransferase EZH2. *Proc. Natl. Acad. Sci. USA* **110**, 7922–7927 (2013).
25. Gil, J. & Peters, G. Regulation of the INK4b-ARF-INK4a tumour suppressor locus: all for one or one for all. *Nat. Rev. Mol. Cell Biol.* **7**, 667–677 (2006).
26. Petitjean, A. *et al.* Impact of mutant p53 functional properties on TP53 mutation patterns and tumor phenotype: lessons from recent developments in the IARC TP53 database. *Hum. Mutat.* **28**, 622–629 (2007).
27. Schroeder, K.M., Hoeman, C.M. & Becher, O.J. Children are not just little adults: recent advances in understanding of diffuse intrinsic pontine glioma biology. *Pediatr. Res.* **75**, 205–209 (2013).
28. Verhaak, R.G.W. *et al.* Integrated genomic analysis identifies clinically relevant subtypes of glioblastoma characterized by abnormalities in PDGFRA, IDH1, EGFR, and NF1. *Cancer Cell* **17**, 98–110 (2010).
29. Pollard, S.M. *et al.* Glioma stem cell lines expanded in adherent culture have tumor-specific phenotypes and are suitable for chemical and genetic screens. *Cell Stem Cell* **4**, 568–580 (2009).
30. Orlando, D.A. *et al.* Quantitative ChIP-Seq normalization reveals global modulation of the epigenome. *Cell Rep.* **9**, 1163–1170 (2014).
31. Deaton, A.M. & Bird, A. CpG islands and the regulation of transcription. *Genes Dev.* **25**, 1010–1022 (2011).
32. Hambardzumyan, D., Amankulor, N.M., Helmy, K.Y., Becher, O.J. & Holland, E.C. Modeling adult gliomas using RCAS/t-va technology. *Transl. Oncol.* **2**, 89–95 (2009).
33. Funato, K., Major, T., Lewis, P.W., Allis, C.D. & Tabar, V. Use of human embryonic stem cells to model pediatric gliomas with H3.3K27M histone mutation. *Science* **346**, 1529–1533 (2014).
34. Zhang, P. *et al.* ABCB1 and ABCG2 restrict the brain penetration of a panel of novel EZH2-Inhibitors. *Int. J. Cancer* **137**, 2007–2018 (2015).

ONLINE METHODS

Expression plasmids. PDGFB expression vector (pCDNA-PDGFB) was a kind gift from L. Uhrbom³⁵ from where PDGFB cDNA was PCR-amplified and cloned into the retroviral expression vector, pMSCV blasticidin. Wild-type and K27M-mutant H3.3 expression vectors were cloned in lentiviral pCDH-CMV-MCS-EF1 puro backbone and were a kind gift from P. Lewis¹⁹. WT *HIST1H3B* (H3.1) cDNA was synthesized by integrated DNA technology (IDT) with a 5' sequence containing an XbaI site and a 3' sequence containing a BamHI site added and delivered in a pUCIDT (Kan) vector. The codon for lysine 27 (AAG) was mutated to the codon for methionine (ATG) by site-directed mutagenesis. H3.1WT or H3.1K27M cDNAs were then cloned into lentiviral pCDH-CMV-H3.3WT-EF1 puro vector using XbaI/BamHI sites. Human constitutively active *EGFR* (**EGFR* or *EGFRvIII*) cloned in retroviral expression vector pMSCV blasticidin was a kind gift from M. van Lohuizen. Human p16^{INK4A} cDNA was cloned in pLVX-TetOne-Puro vector (Clontech Laboratories).

Cell lines and culture. NSCs were isolated from the dorsal forebrain of embryonic-day 12.5 (E12.5) mouse embryos. E12.5 embryos were isolated, and, after removal of the skin, dorsal forebrains were dissected out and incubated with 0.25% trypsin-EDTA (GIBCO) at 37 °C for 20 min. The tissue was dissociated thoroughly with pipette, spun down, washed and cultured on poly-D-lysine (PDL, Sigma-Aldrich)- and laminin (Sigma-Aldrich)-coated plates in neural stem cell medium (50% DMEM-F12, 50% neurobasal medium, N2 and B27 supplements, sodium pyruvate, glutamax, HEPES, β -mercaptoethanol, non-essential amino acids, bovine serum albumin, heparin, 100 U/ml penicillin, 100 μ g/ml streptomycin, human recombinant epidermal and basic fibroblast growth factors). After 2–3 d, the expanded cells were trypsinized and frozen down in NSC medium supplemented with 10% DMSO. *Ink4a/Arf*^{-/-} and *Trp53*^{-/-} NSCs were derived from embryos isolated from crosses between heterozygous mice.

SF7761 and SF8628 primary DIPG cells were a kind gift from N. Gupta³⁶ and were isolated from biopsied tissue from patients with DIPG. All cell lines in the DIPG and GBM series are derived from the Hospital Sant Joan de Déu Barcelona, Spain. DIPG007 (HSJD-DIPG-007) cells were obtained from the autopsy of a 9.9-year-old boy, who survived less than 1 month after diagnosis, after having received one cycle of irinotecan–cisplatin and no radiation therapy. It was a glioblastoma multiforme (WHO grade IV). HSJD-DIPG-012 was obtained from a biopsy at diagnosis (no treatment of any kind) in a 9.7-year-old boy. It was an anaplastic astrocytoma (WHO grade III). The patient survived 1.2 years after diagnosis. SF7761, DIPG007 and DIPG012 cells were cultured in NSC medium described above whereas SF188 and SF8628 cells were cultured in Dulbecco's modified Eagle's medium (DMEM) supplemented with 10% FBS, 100 U/ml penicillin and 100 μ g/ml streptomycin.

Primary GNS cells (G14, G26, G144 and G166) were a kind gift from S.M. Pollard²⁹ and were cultured in NSC medium. All cell lines used were tested and confirmed to be negative for mycoplasma.

Virus production and transduction. For production of retroviruses and lentiviruses, expression vectors were transfected in Phoenix-Eco or 293FT cells, respectively, using calcium phosphate method. After 8 h, cells were washed and cultured in desired medium. After 48 h, the medium was collected and passed through a 0.45- μ m filter. For transduction, the cells were cultured in medium containing virus particles supplemented with polybrene. After 48 h of transduction, cells were harvested and cultured in the selection medium.

Stereotactic injection in mice. All mouse experiments were approved by the Danish animal-welfare authority. The stereotactic injections in severe combined immunodeficient (SCID) mice (Harlan Laboratories) were performed as previously described³⁷. Briefly, 6–10-week-old female SCID mice were anesthetized using isoflurane (1.5 l O₂/minute and 2.5% isoflurane) and placed in a stereotactic device (David Kopf instruments). A small incision was made to expose the skull, and a 0.5-mm small hole was drilled in the skull 0.8-mm below and 1-mm left to the lambda. 10,000 cells in a 5- μ l volume were injected 5 mm below the skull using a microsyringe (Agnthos) at a rate of 2 μ l/minute. The hole in the skull was closed with bonewax (Agnthos), and the scalp was closed using clips (Agnthos). The clips were removed 1 week after injection.

Immunohistochemistry. Tumor-bearing mice were killed, whole brains were washed with PBS and fixed in 4% formaldehyde for 24 h at 4 °C. Tissues were processed, paraffin-embedded and cut into 5- μ m sections. Sections were deparaffinized by incubating at 60 °C for 20 min, cleared in Xylene and passed through a series of graded alcohols.

For H&E, slides were stained with Mayer's hematoxylin (Sigma-Aldrich) for 2 min, blued in 0.1% sodium bicarbonate for 1 min, washed in water and counterstained with Eosin Y solution (Sigma-Aldrich) for 1 min.

For immunohistochemistry (IHC), sections were heat-activated with antigen-retrieval buffer (0.1 M Na-citrate buffer, 0.05% Tween, pH 6) at 95–100 °C for 50 min. After cooling, slides were blocked with blocking solution (2% goat serum, 2% BSA, 0.05% Tween in PBS) for 1 h at room temperature and incubated overnight with primary antibody diluted in blocking solution. After two washes in PBS-Tween, endogenous peroxidase-activity was quenched with 0.3% H₂O₂ in PBS-Tween for 15 min. Slides were washed twice in PBS-Tween and incubated with HRP-conjugated secondary antibody (EnVision, Dako) for 1 h at room temperature. Slides were washed three times for 5 min with PBS-Tween, developed with DAP substrate (NovaRED, Vector Labs) for 5 min, counterstained and blued with hematoxylin, dehydrated with a series of graded alcohols and mounted in a Xylene-based mounting medium (Vectashild, Vector Labs). Slides were scanned using a NanoZoomer from Hamamatsu.

Protein extraction and immunoblotting. Cells were trypsinized, washed once with phosphate-buffered saline (PBS) and lysed in TOPEX+ buffer (300-mM NaCl, 50-mM Tris-HCl pH 7.5, 0.5% Triton X-100, 1% SDS, 1-mM DTT, aprotinin, leupeptin, 0.1-mM phenylmethanesulfonyl fluoride (PMSF) and 33.33 U/ml benzamide (EMD-Novagen)). Protein concentrations were measured by Bradford reagent (Bio-Rad). Cell lysates were separated by SDS-PAGE and transferred to nitrocellulose membrane. Full images of immunoblots are shown in **Supplementary Figures 10–13**.

Chromatin immunoprecipitation (ChIP) and library preparation for sequencing.

Cells were cross-linked with 1% formaldehyde for 10 min at room temperature. Glycine was added at a final concentration of 125 mM to quench the formaldehyde. Cells were then washed twice with PBS and harvested in SDS buffer (50 mM Tris at pH 8.1, 0.5% SDS, 100-mM NaCl, 5-mM EDTA). Cells were spun down, resuspended in Triton-X IP buffer (100-mM Tris at pH 8.6, 0.3% SDS, 1.7% Triton X-100 and 5-mM EDTA) and the chromatin was sonicated to get the DNA fragments of <1,000 bp with average DNA fragment size of 300 bp. 100 μ g of chromatin was pre-cleared with protein A Sepharose beads (GE healthcare) for 1–2 h and incubated with the antibody overnight at 4 °C. 1 d later, protein A Sepharose beads were added and incubated for 3 h at 4 °C. Beads were washed three times with low-salt buffer (1% Triton X-100, 0.1% SDS, 150-mM NaCl, 2-mM EDTA, pH 8.0, 20-mM Tris-HCl, pH 8.0) and once with high-salt buffer (1% Triton X-100, 0.1% SDS, 500-mM NaCl, 2-mM EDTA, pH 8.0, 20-mM Tris-HCl, pH 8.0). Beads were incubated with elution buffer (1% SDS, 0.1 M sodium bicarbonate) at 65 °C for 4 h to overnight to elute to the immune complexes. The DNA was isolated and purified using QIAquick PCR purification kit (Qiagen) and eluted in 100 μ l elution buffer. The ChIP DNA was diluted ten times in water and subjected to qPCR analysis using 1X SYBR green master mix (Roche Applied Science) and LightCycler 480 instrument (Roche Applied Science). The primers used for the analysis are listed in **Supplementary Table 4**.

For ChIP-seq, 500 μ g of chromatin was used to perform ChIP, and the purified ChIP DNA was quantified using Qubit Fluorometer (Life Technologies). 10 ng of ChIP DNA was used to make library using NEBNext Ultra DNA library kit for Illumina (E7370; New England Biolabs), according to the supplier's instructions, and the libraries were sequenced using an Illumina HiSeq2500 sequencer.

Cell-proliferation assay. 100,000–200,000 cells were plated in duplicate in six-well plates and treated with either DMSO or EZH2 inhibitors (GSK343 and EPZ6438, 3 μ M). Cells were harvested and counted using Neubauer chamber every 3–4 d.

Cell-cycle analysis. Cell-cycle analysis was performed using Click-iT EdU assay kit (Life Technologies), according to the supplier's instructions. In brief, the cultured cells were treated with 10 μ M EdU for 30–60 min, washed once with 1% BSA in PBS and fixed with 4% paraformaldehyde in PBS for 15 min at room temperature. Fixed cells were permeabilized and incubated with the fluorescent

dye azide for 30 min at room temperature. The cells were then washed, resuspended in the permeabilization buffer containing propidium iodide and analyzed using flow cytometry.

β -galactosidase assay. The assay to detect β -galactosidase was performed as previously described³⁸. In brief, cells were washed with PBS twice and fixed in 2% formaldehyde and 0.2% glutaraldehyde for 5 min at room temperature. Fixed cells were washed and incubated with a staining solution containing 1 mg/ml X-gal at 37 °C overnight.

Analysis of pediatric GBM and DIPG samples. Written informed consent was received from all patients before inclusion of their samples in the Hospital Sant Joan de Déu (HSJD) tumor biobank. Our internal review board approved the studies performed in this study.

Immunohistochemical analyses were performed by following standard techniques with heat-induced antigen retrieval with sodium citrate and using an indirect immunoperoxidase method. The primary antibodies used were mouse anti-p53 (DO-1) (1:100, Novocastra), mouse H3K27me3 (1:500, Abcam) and mouse anti-p16 (DCS-50). Staining was visualized with Novolink Polymer detection Systems from Leica, followed by hematoxylin counterstaining.

Fluorescent *in situ* hybridization (FISH) analysis of *CDKN2A* (9p21) was performed by dual-color probes on 2- μ m sections derived from formalin-fixed paraffin-embedded (FFPE) samples digested with proteinase K at 37 °C for 15 min. Slides were hybridized with a p16 (9p21)-specific DNA Probe (KBI-10710, Leica biosystems) overnight in a 37 °C humidified chamber, washed the following day and counterstained with DAPI. Mounted slides were subsequently analyzed by Leica fluorescence microscopy.

Sequencing of *H3F3A* and *HIST1H3B* was performed according to previously reported method¹⁵. Copy-number variation (CNV) analysis was performed using the high-density genome-wide CytoScan HD platform (Affymetrix, Thermo Fischer Scientific). DNA was extracted from fresh-frozen tumor biopsies with more than 70%-viable tumor-cell content using standard procedures. Analysis of the CytoScan HD Array data was performed using the Chromosome Analysis Suite (ChAS) software (Affymetrix Thermo Fischer Scientific).

TRP53 sequencing was performed by automated sequencing (Applied Biosystems 3730 DNA Analyzer) of the entire coding sequence of the *TRP53* gene (exon 1–11) using Big Dye Terminator v3.1 Cycle Sequencing kit (Applied Biosystems, US), following standard protocols.

Generation of p16^{INK4A}/p14^{ARF}-knockout DIPG cell line using CRISPR–Cas9. Small guide RNA was designed to target the second exon (common to *INK4A* and *ARF*, gRNA target sequence: 5'-GACCCGTGCACGACGCTGCC-3') and cloned into pSpCas9(BB)-2A-GFP (Addgene plasmid ID: 48138), as previously described³⁹. DIPG007 cells were transfected using an Amaxa Nucleofector II (program A033). Single-GFP-expressing cells were sorted into multi-well dishes 24 h after transfection. Gene targeting was confirmed by PCR amplification (5' primer-TCTGACCATTCTGTTCTCTCTGG, 3' primer-TCTCAGATCA TCAGTCTCTACCT), followed by cloning into TOPO/pCR8 (ThermoFisher Scientific) and Sanger sequencing.

Genotyping of tumors. Tumors were isolated and treated with Proteinase K in TENES buffer (10-mM Tris, pH 7.5, 400-mM NaCl, 100-mM EDTA, 0.6% SDS) for 4 h to overnight, and DNA was isolated using phenol-chloroform extraction. PCR was performed using primers listed in **Supplementary Table 4**.

Histone isolation and digestion. Histones were acid extracted as previously described⁴⁰.

Middle-down LC–MS/MS and data analysis. The middle-down liquid chromatography tandem–mass spectrometry (LC–MS/MS) analysis was performed as described in ref. 41.

Targeted bottom-up LC–MS/MS and data analysis. For targeted bottom-up LC–MS/MS analysis, histones were derived using propionic anhydride and digested with trypsin (1:10 w/w enzyme to substrate ratio), as previously described⁴². Peptide mixtures were separated by on-line chromatography using EASY-nLC 1200 nanoHPLC system (Thermo scientific). The nanoLC was equipped with

a two-column setup, a 4-cm precolumn (100- μ m ID) and 15-cm analytical column, both in-house packed with C₁₈ bulk material (ReproSil, Pur C18AQ 1.9 μ m; Dr. Maisch). The HPLC gradient was 0–34% buffer B (A = 0.1% formic acid; B = 95% acetonitrile, 0.1% formic acid) over 20 min and from 34% to 100% buffer B in 5 min at a flow-rate of 250 nl/min. LC was coupled with a Q Exactive HF mass spectrometer (Thermo Fisher Scientific). The spray voltage was 2.3 kV, and the capillary temperature was 275 °C. Data acquisition was performed at high-mass resolution in the Orbitrap for both precursor and product ions, with a mass resolution of 120,000 for MS and 15,000 for MS/MS. The spectra were acquired as follows: a selected-ion monitoring (SIM) scan (automatic gain control (AGC) target 3×10^6 , 200-ms maximum injection time, *m/z* 490–820) was followed by nine parallel reaction monitoring (PRM) scans (AGC target 2×10^5 , 100-ms maximum injection time) triggered by an inclusion list. The inclusion list contained peptides covering residues 27–40 of histones H3.1/2, H3.3, and H3.3K27M, as well as their post-translationally modified forms. The spectra were searched using Mascot v2.3 (Matrix Science). Mono- and dimethylation (KR), trimethylation (K) and acetylation (K) were set as variable modifications, and propionylation (K) was set as a static modification. Each histone proteoform was quantified on the basis of the precursor ion intensity, using Skyline software. The relative abundance of H3.3K27M mutant was calculated as the sum of abundances of all H3.3K27M peptides, including modified forms, divided by the sum of abundances of all H3 peptides.

Soft-agar colony formation. Soft-agar colony formation was performed in a 12-well plate in which 2,000 cells in NSC medium containing 0.3% low-melting agarose (LMP, Life Technologies) were plated in triplicate on top of the solidified layer of 0.7% LMP in NSC medium. On the next day of plating, the NSC medium was added to each well, and the medium was replaced every third day. Colonies formed after 10–11 d were pictured by inverted microscope and counted by ImageJ. Cell viability was measured using PrestoBlue reagent (ThermoFisher Scientific) according to the manufacturer's protocol.

Computational procedures. Detailed computational procedures are available in **Supplementary Methods**.

Code availability. Scripts used for data analyses are available on request.

Statistical analyses. All statistical analyses were performed using GraphPad Prism 6 (GraphPad Software, San Diego, CA). A log-rank test was performed to analyze Kaplan–Meier survival curves. Proliferation assays were performed in triplicate, and data were represented as \pm s.d. Nonlinear-regression fit analyses were performed to compare the slopes of different proliferation curves. Data sets represented as bar graphs were compared using two-tailed unpaired Student's *t*-test, assuming that the data are normally distributed and have equal variance. To compare more than two data sets, as in **Supplementary Figure 3c**, an ordinary two-way ANOVA test was performed. Data in **Supplementary Figure 9c** were not normally distributed, and thus a Kolmogorov Smirnov test was used to compare cumulative distribution. Sample size was empirically determined.

Data availability. ChIP-seq and RNA-seq data are available at the Gene Expression Omnibus (GEO) under accession [GSE85390](https://www.ncbi.nlm.nih.gov/geo/query/acc.cgi?acc=GSE85390).

35. Jiang, Y., Boije, M., Westermark, B. & Uhrbom, L. PDGF-B Can sustain self-renewal and tumorigenicity of experimental glioma-derived cancer-initiating cells by preventing oligodendrocyte differentiation. *Neoplasia* **13**, 492–503 (2011).
36. Hashizume, R. *et al.* Characterization of a diffuse intrinsic pontine glioma cell line: implications for future investigations and treatment. *J. Neurooncol.* **110**, 305–313 (2012).
37. Caretti, V. *et al.* Monitoring of tumor growth and post-irradiation recurrence in a diffuse intrinsic pontine glioma mouse model. *Brain Pathol.* **21**, 441–451 (2011).
38. Debacq-Chainiaux, F., Erusalimsky, J.D., Campisi, J. & Toussaint, O. Protocols to detect senescence-associated beta-galactosidase (SA-beta-gal) activity, a biomarker of senescent cells in culture and in vivo. *Nat. Protoc.* **4**, 1798–1806 (2009).
39. Ran, F.A. *et al.* Genome engineering using the CRISPR-Cas9 system. *Nat. Protoc.* **8**, 2281–2308 (2013).
40. Shechter, D., Dormann, H.L., Allis, C.D. & Hake, S.B. Extraction, purification and analysis of histones. *Nat. Protoc.* **2**, 1445–1457 (2007).
41. Sidoli, S. *et al.* Middle-down hybrid chromatography/tandem mass spectrometry workflow for characterization of combinatorial post-translational modifications in histones. *Proteomics* **14**, 2200–2211 (2014).
42. Lin, S. & Garcia, B.A. Examining histone posttranslational modification patterns by high-resolution mass spectrometry. *Methods Enzymol.* **512**, 3–28 (2012).